14th ITP/CAS–BLTP/JINR Joint Workshop on Physics of Strong Interacting Systems

18–23 October 2026 Nanjing, China

Role of the Scission-Line Structure in the Formation of the ^{180}Hg Fission-Fragment Mass Distribution



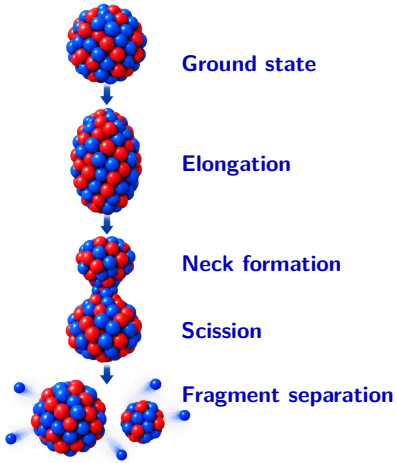
Jin-Tian Liu

Institute of Theoretical Physics, Chinese Academy of Sciences

Collaborators: A. Rahmatinejad, J. Zhao, T. M. Shneidman, N. V. Antonenko, and S.-G. Zhou

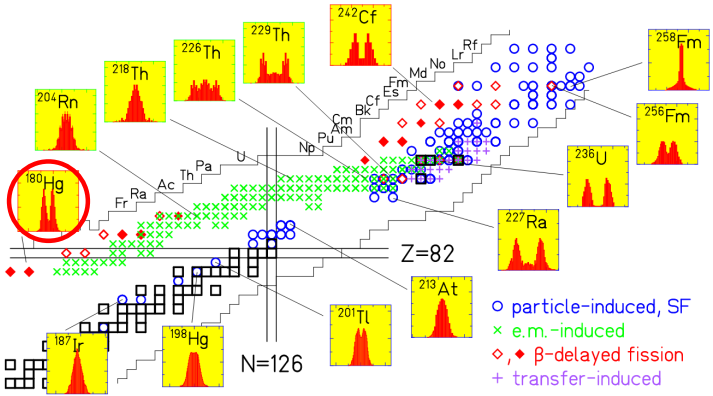
Motivation: fission yields and total kinetic energies

- **Probe nucleon partitioning**: Mass and charge yields reveal how nucleons divide between fragments and test the roles of shell structure, pairing correlations, and shape evolution.
- **Constrain energy sharing and scission dynamics**: Total kinetic energy and its correlation with yields constrain scission configurations, dissipation, fragment excitation, and subsequent neutron emission.
- **Support nuclear technology and isotope applications**: Reliable energy-dependent yields inform reactor design, nuclear-waste management, and fission-product applications.
- **Connect to other fundamental problems**: Fission yields affect matter recycling and abundances in the r process; β decay of fission products shapes reactor antineutrino spectra.



J. Pei, Y. Qiang, and C. Qiao, Physics **51**, 770–777 (2022) (in Chinese).

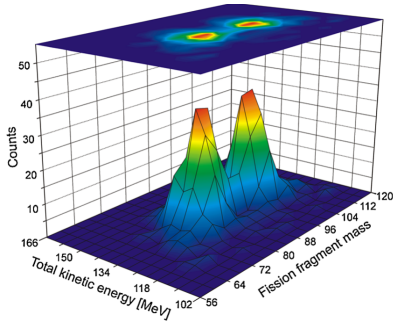
Typical fission modes observed experimentally



K.-H. Schmidt and B. Jurado, Rep. Prog. Phys. **81**, 106301 (2018).

Why does ^{180}Hg split asymmetrically near $80/100$?

- The liquid-drop model suggests a symmetric split
$$^{180}\mathrm{Hg} \longrightarrow {}^{90}\mathrm{Zr} + {}^{90}\mathrm{Zr}.$$
- ^{90}Zr has the neutron magic number $N = 50$ and the proton semi-magic number $Z = 40$.
- Beta-delayed fission of ^{180}Tl instead reveals an asymmetric split:
$$^{180}\mathrm{Tl} \xrightarrow{\mathrm{EC}} {}^{180}\mathrm{Hg}^{*} \xrightarrow{\text{fission}} F_{\mathrm{L}} + F_{\mathrm{H}}$$
$$A_{\mathrm{L}}/A_{\mathrm{H}} \simeq 80/100.$$



Experimental fragment-mass and TKE distributions

A. N. Andreyev et al., Phys. Rev. Lett. **105**, 252502 (2010).

Previous theoretical studies of ^{180}Hg fission

Macroscopic–microscopic models

Brownian shape-motion model
Stochastic shape evolution on a five-dimensional potential-energy surface. The predicted mass split is $A_{\mathrm{H}}/A_{\mathrm{L}} = 108/72$.
P. Möller et al., Phys. Rev. C **85**, 024306 (2012).

Scission-point model
Yields are calculated from statistical weights of scission configurations, giving a split near $95/85$.
A. V. Andreev et al., Phys. Rev. C **88**, 047604 (2013).

Microscopic models

Nonrelativistic mean field
Skyrme-HFB (SkM*) and Gogny-HFB (D1S) calculations examine deformation-energy surfaces and prefragment structure.
M. Warda et al., Phys. Rev. C **86**, 024601 (2012).

Relativistic framework
TDGCM+GOA describes collective wave-packet evolution in a relativistic mean-field framework and predicts fission-fragment mass distributions.
Z. Y. Li et al., Phys. Rev. C **106**, 024307 (2022).

Models differ in shape space, dynamics, and scission criteria.

How does the scission-line structure affect the mass distribution?

Theoretical framework: Relativistic Hartree–Bogoliubov (RHB) model

Point-coupling Lagrangian density

$$\mathcal{L} = \mathcal{L}_0 + \mathcal{L}_{4\mathrm{f}} + \mathcal{L}_{\mathrm{nl}} + \mathcal{L}_{\mathrm{der}} + \mathcal{L}_{\mathrm{em}}$$

$$\mathcal{L}_0 = \bar{\psi}(i\gamma^\mu\partial_\mu - M)\psi,$$

$$\mathcal{L}_{4\mathrm{f}} = -\frac{1}{2}\alpha_{\mathrm{S}}\rho_{\mathrm{S}}^2 - \frac{1}{2}\alpha_{\mathrm{V}}\rho_{\mathrm{V}}^2 - \frac{1}{2}\alpha_{\mathrm{TS}}\rho_{\mathrm{TS}}^2 - \frac{1}{2}\alpha_{\mathrm{TV}}\rho_{\mathrm{TV}}^2,$$

$$\mathcal{L}_{\mathrm{nl}} = -\frac{1}{3}\beta_{\mathrm{S}}\rho_{\mathrm{S}}^3 - \frac{1}{4}\gamma_{\mathrm{S}}\rho_{\mathrm{S}}^4 - \frac{1}{4}\gamma_{\mathrm{V}}(\rho_{\mathrm{V}}^2)^2,$$

$$\mathcal{L}_{\mathrm{der}} = -\frac{1}{2}\delta_{\mathrm{S}}(\partial_\nu\rho_{\mathrm{S}})^2 - \frac{1}{2}\delta_{\mathrm{V}}(\partial_\nu\rho_{\mathrm{V}})^2 - \frac{1}{2}\delta_{\mathrm{TS}}(\partial_\nu\rho_{\mathrm{TS}})^2 - \frac{1}{2}\delta_{\mathrm{TV}}(\partial_\nu\rho_{\mathrm{TV}})^2,$$

$$\mathcal{L}_{\mathrm{em}} = -\frac{1}{4}F^{\mu\nu}F_{\mu\nu} - e\frac{1-\tau_3}{2}A_\mu J_{\mathrm{V}}^\mu.$$

A. Bouyssy et al., Phys. Rev. C **36**, 380 (1987).
B. A. Nikolaus et al., Phys. Rev. C **46**, 1757 (1992).
P. Bernardos et al., Phys. Rev. C **48**, 2665 (1993).
P. Ring, Prog. Part. Nucl. Phys. **37**, 193 (1996).
T. Bürvenich et al., Phys. Rev. C **65**, 044308 (2002).

RHB equation

$$\int d^3\boldsymbol{r}' \begin{pmatrix} h_{\mathrm{D}} - \lambda & \Delta \\ -\Delta^* & -h_{\mathrm{D}}^* + \lambda \end{pmatrix} \begin{pmatrix} U_k \\ V_k \end{pmatrix} = E_k \begin{pmatrix} U_k \\ V_k \end{pmatrix}$$

$$h_{\mathrm{D}} = \boldsymbol{\alpha}\cdot\boldsymbol{p} + \beta[M + S(\boldsymbol{r})] + V(\boldsymbol{r})$$

$$S(\boldsymbol{r}) = \alpha_{\mathrm{S}}\rho_{\mathrm{S}} + \alpha_{\mathrm{TS}}\boldsymbol{\rho}_{\mathrm{TS}}\cdot\boldsymbol{\tau} + \beta_{\mathrm{S}}\rho_{\mathrm{S}}^2 + \gamma_{\mathrm{S}}\rho_{\mathrm{S}}^3 + \delta_{\mathrm{S}}\Delta\rho_{\mathrm{S}} + \delta_{\mathrm{TS}}\Delta\boldsymbol{\rho}_{\mathrm{TS}}\cdot\boldsymbol{\tau},$$

$$V(\boldsymbol{r}) = \alpha_{\mathrm{V}}\rho_{\mathrm{V}} + \alpha_{\mathrm{TV}}\boldsymbol{\rho}_{\mathrm{TV}}\cdot\boldsymbol{\tau} + \gamma_{\mathrm{V}}\rho_{\mathrm{V}}^3 + \delta_{\mathrm{V}}\Delta\rho_{\mathrm{V}} + \delta_{\mathrm{TV}}\Delta\boldsymbol{\rho}_{\mathrm{TV}}\cdot\boldsymbol{\tau} + e\frac{1-\tau_3}{2}A^0.$$

The RHB model treats the nucleonic mean field and pairing correlations self-consistently.

Shape parametrization and multidimensionally constrained CDFT

Shape parametrization

$$R(\theta,\varphi) = R_0\left[1+\beta_{00}+\sum_{\lambda=1}^{\infty}\sum_{\mu=-\lambda}^{\lambda}\beta^*_{\lambda\mu}Y_{\lambda\mu}(\theta,\varphi)\right].$$

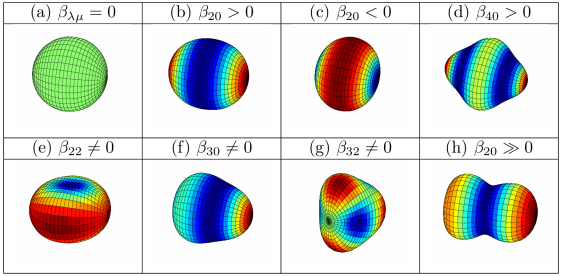
β_{20}, β_{22}, and β_{30} describe axial quadrupole, triaxial quadrupole, and axial octupole deformations, respectively.

Multidimensionally constrained covariant density functional theory (MDC-CDFT)

$$E' = E_{\mathrm{RMF}} + \sum_{\lambda\mu} C_{\lambda\mu}\beta_{\lambda\mu}$$

$$\langle\hat{Q}_{\lambda\mu}\rangle = \int d^3\boldsymbol{r}\,\rho_{\mathrm{V}}(\boldsymbol{r})r^{\lambda}Y_{\lambda\mu}(\Omega), \qquad \beta_{\lambda\mu} = \frac{4\pi}{3AR^{\lambda}}\langle\hat{Q}_{\lambda\mu}\rangle.$$

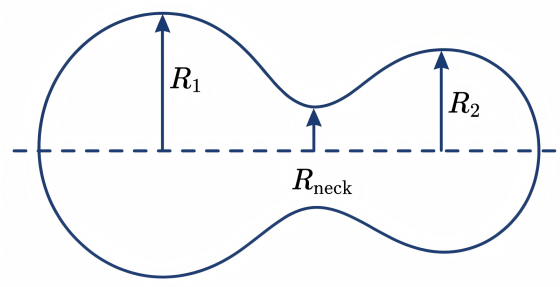
All deformation modes allowed by V_4 symmetry can be included self-consistently.



Deformation degrees of freedom in the multipole expansion

B. N. Lu, Ph.D. thesis, ITP-CAS (2012).
B. N. Lu et al., Phys. Rev. C **85**, 011301 (2012).
B. N. Lu et al., Phys. Rev. C **89**, 014323 (2014).
J. Zhao et al., Phys. Rev. C **92**, 064315 (2015).
S.-G. Zhou, Phys. Scr. **91**, 063008 (2016).
J. Zhao et al., Phys. Rev. C **95**, 014320 (2017).

Definition of scission and fragment partitioning



Geometric scission criterion

$$\rho(r,z) = 0.10\,\mathrm{fm}^{-3}, \quad R_{\mathrm{neck}} \le 1.0\,\mathrm{fm}$$

First qualifying point at each β_{30} as β_{20} increases.

Density-based partition coordinate

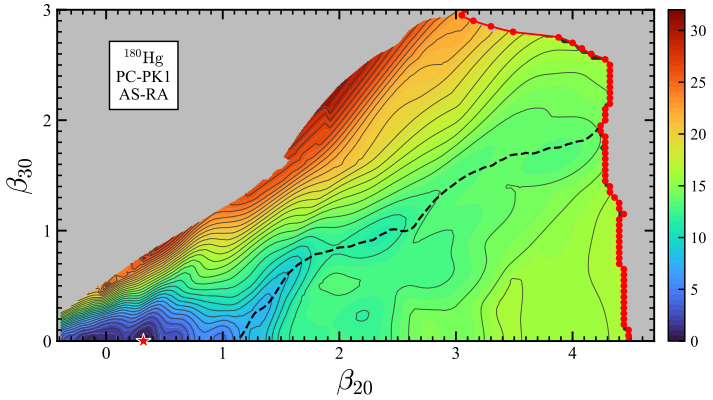
$$\mathcal{N}(z) = \int_{z_{\min}}^{z_{\max}} e^{-(z'-z)^2/a_{\mathrm{neck}}^2}\,\varrho_A(z')\,dz'$$

$$\boxed{\mathcal{N}'(z_{\mathrm{div}}) = 0, \qquad \mathcal{N}''(z_{\mathrm{div}}) > 0}$$

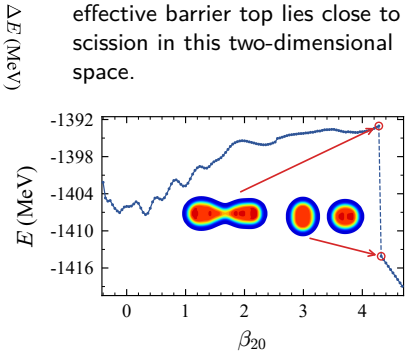
ϱ_A: total line density; $a_{\mathrm{neck}} = 1.0\,\mathrm{fm}$.
Minimum between the two fragment-density peaks.

$$A_{\mathrm{L}} = 2\pi \int_{-\infty}^{z_{\mathrm{div}}} dz \int_0^{\infty} \rho(r,z)\, r\, dr, \qquad A_{\mathrm{L}} + A_{\mathrm{H}} = 180$$

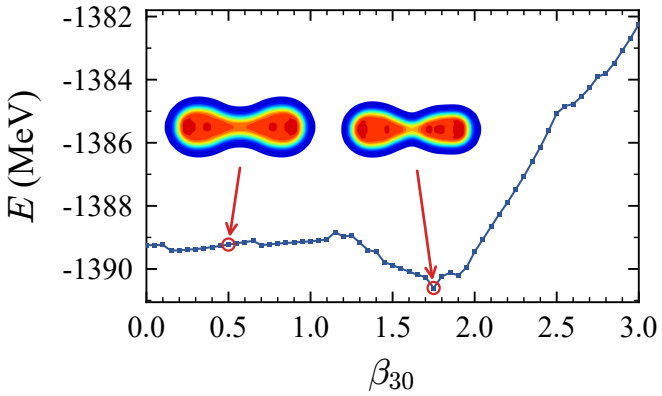
Potential-energy surface and static fission path



- The low-energy valley favors asymmetric shapes, while the symmetric branch forms a high-energy ridge.
- Along the static path, the effective barrier top lies close to scission in this two-dimensional space.



Energy variation along the scission line



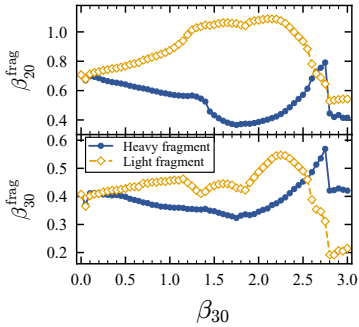
The detailed energy structure of the scission boundary is crucial for the fragment mass distribution.

- The minimum energy along the scission line occurs at

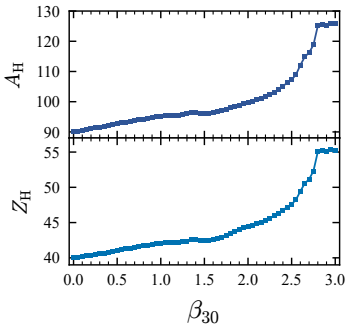
$$\beta_{30} \simeq 1.7\text{–}1.8.$$

- Scission configurations with finite octupole deformation are energetically favored.

Prefragment properties at scission



Heavy fragment: filled circles, solid lines
Light fragment: open diamonds, dashed lines



$\beta_{30} = 1.7$–1.8: $A_{\mathrm{H}} \approx 97$–$98$, $Z_{\mathrm{H}} \approx 43$

- The prefragments exhibit **substantial quadrupole and octupole deformations**, and the resulting scission configurations differ markedly from the symmetric fission predicted by the liquid-drop model.
- We calculate the prefragment mass and charge numbers for use in the subsequent mass-distribution calculation.

Finite-temperature Bardeen–Cooper–Schrieffer (FT–BCS) equations

Finite-temperature BCS equations

$$E_k^\tau(T_q,q) = \left[\left(\varepsilon_k^\tau(q) - \lambda_\tau(T_q,q)\right)^2 + \Delta_\tau^2(T_q,q)\right]^{1/2}$$

$$N_\tau = \sum_{k>0}\left[1 - \frac{\varepsilon_k^\tau(q) - \lambda_\tau(T_q,q)}{E_k^\tau(T_q,q)}\tanh\left(\frac{E_k^\tau(T_q,q)}{2T_q}\right)\right],$$

$$\frac{2}{G_\tau(q)} = \sum_{k>0}\frac{1}{E_k^\tau(T_q,q)}\tanh\left(\frac{E_k^\tau(T_q,q)}{2T_q}\right).$$

At each deformation point, the local temperature describes intrinsic excitation built on RHB calculation.

A. Rahmatinejad et al., Phys. Rev. C **103**, 034309 (2021).
A. Rahmatinejad et al., Phys. Rev. C **105**, 044328 (2022).
A. Rahmatinejad et al., Eur. Phys. J. A **60**, 214 (2024).

Excitation energy, entropy, and level density

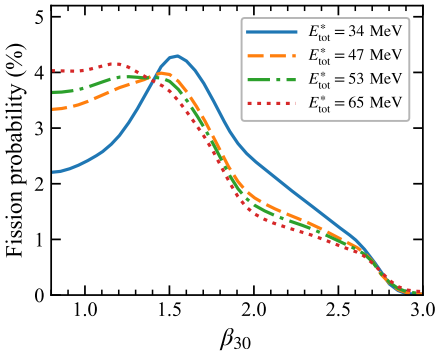
$$U_\tau(T_q,q) = \mathcal{E}_\tau(T_q,q) - \mathcal{E}_\tau(0,q).$$

$\mathcal{E}_\tau$ follows from the self-consistent finite-temperature BCS solution.

$$S_\tau(T_q,q) = 2\sum_{k>0}\left[\ln\left(1+\mathrm{e}^{-E_k^\tau(T_q,q)/T_q}\right) + \frac{E_k^\tau(T_q,q)/T_q}{1+\mathrm{e}^{E_k^\tau(T_q,q)/T_q}}\right]$$

$$\boxed{\rho_{\mathrm{int}}(U,N,Z;q) = \frac{\exp[S(U,N,Z;q)]}{(2\pi)^{3/2}\mathcal{D}}}$$

Excitation-energy dependence of the scission probability distribution



Equilibrium probability along the scission line

$$P^{\rm eq}(i_s) = \frac{\rho_{i_s}}{\sum_{i'_s \in \mathcal{S}} \rho_{i'_s}}$$

$$\frac{P^{\rm eq}(i_s)}{P^{\rm eq}(i'_s)} = \frac{\rho_{i_s}}{\rho_{i'_s}}$$

- At low excitation energy, the probability is concentrated near $\beta_{30} \simeq 1.5$.
- As the excitation energy increases, the distribution broadens and shifts toward smaller β_{30}.
- The relative weights of neighboring configurations vary with excitation energy.

Level densities determine the statistical weights of scission configurations

Master equation: from shape evolution to scission probabilities

Deformation grid q_i → Master equation $P_i(t)$ → Scission line $\mathcal{S}$ → Mass yield $Y(A)$

1. Statistical weight of each configuration

$$q_i = (\beta_{20}, \beta_{30})$$
$$U_i = E^* - V(q_i)$$
$$\rho_i = \rho_{\rm int}(U_i, N, Z; q_i)$$

2. Transitions between neighboring configurations

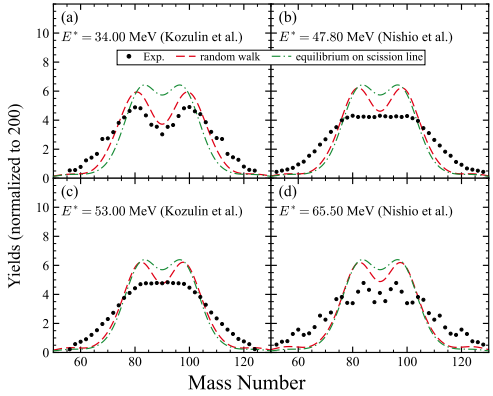
$$\frac{dP_i}{dt} = \sum_j (\Lambda_{ij} P_j - \Lambda_{ji} P_i)$$
$$\Lambda_{ij} = \frac{2\pi}{\hbar} \left| \langle i | \hat{V} | j \rangle \right|^2 \rho_i$$
$$\Lambda_{ij} = \lambda \sqrt{\rho_i / \rho_j} \qquad (j \to i)$$

3. Scission probability and equilibrium reference

$$\mathcal{P}(i_s) = \int_0^\infty dt \sum_{j \notin \mathcal{S}} \Lambda_{i_s j} P_j(t)$$
$$P^{\rm eq}(i_s) = \frac{\rho_{i_s}}{\sum_{i'_s \in \mathcal{S}} \rho_{i'_s}}$$

A. Rahmatinejad et al., Phys. Rev. C **103**, 034309 (2021).
A. Rahmatinejad et al., Phys. Rev. C **105**, 044328 (2022).

Calculated and experimental mass distributions



Red dashed: random walk
Green dash-dotted: scission-line equilibrium
Black symbols: experiment; both calculations use $\sigma_A = 4.0$ u.

- Across $E^* = 34.0$–65.5 MeV, the main peaks remain near $80/100$.
- The symmetric component grows with excitation energy, but the **asymmetric mode remains dominant**.
- At higher energies, the calculations converge, although discrepancies remain in the peak heights and tails.

K. Nishio et al., Phys. Lett. B **748**, 89 (2015).

E. M. Kozulin et al., Phys. Rev. C **105**, 014607 (2022).

Summary and outlook

Summary

- We calculate the $^{180}\mathrm{Hg}$ potential-energy surface with MDC-RHB and combine master-equation shape evolution with prefragment properties to describe asymmetric fission.
- The reflection-asymmetric valley and the scission boundary defined by self-consistent densities and a geometric neck criterion favor strongly deformed prefragments and yield the observed $A_{\mathrm{L}}/A_{\mathrm{H}} \simeq 80/100$ split.
- Both the master-equation and scission-line equilibrium calculations retain the asymmetric preference, demonstrating the key role of the energy structure along the scission line.

Outlook

- Future work will include collective inertia, higher-order shape fluctuations, and post-scission neutron emission, and will test this mechanism in neutron-deficient Hg, Pb, and Pt nuclei.

Thank you!

Backup: construction and scope of the mass yield

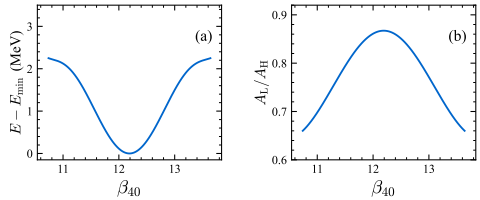
From scission probabilities to the mass yield

$$Y(A) = 100 \sum_{i_s \in \mathcal{S}} \mathcal{P}(i_s) \left[G_{\sigma_A}(A - A_{\mathrm{L},i_s}) + G_{\sigma_A}(A - A_{\mathrm{H},i_s}) \right]$$

$$G_{\sigma_A}(x) = \frac{e^{-x^2/(2\sigma_A^2)}}{\sqrt{2\pi}\sigma_A}, \qquad \sigma_A = 4.0\,\mathrm{u}$$

- Each fission event contributes one light and one heavy fragment; the total yield is normalized to 200.
- The random walk uses cumulative first-arrival probabilities at the absorbing boundary, while the equilibrium result uses level-density weights along the scission line.
- The β_{40} scan supports the presence of mass fluctuations but does not uniquely determine the Gaussian width.
- The present broadening is phenomenological and does not yet include the full higher-dimensional fluctuations or post-scission neutron emission.

Appendix: hexadecapole fluctuations and mass broadening



From scission configurations to the mass yield

$$Y(A) = 100 \sum_{i_s \in \mathcal{S}} \mathcal{P}(i_s) \left[G_{\sigma_A}(A - A_{\mathrm{L},i_s}) + G_{\sigma_A}(A - A_{\mathrm{H},i_s}) \right]$$

$$G_{\sigma_A}(x) = \frac{e^{-x^2/(2\sigma_A^2)}}{\sqrt{2\pi}\sigma_A}, \qquad \sigma_A = 4.0\,\mathrm{u}$$ L. G. Moretto and J. Sventek, Phys. Lett. B **58**, 26 (1975).

- At fixed $(\beta_{20}, \beta_{30}) = (4.28, 1.60)$, we additionally constrain the hexadecapole deformation β_{40}.
- Within the converged interval, $A_{\mathrm{H}} \approx 96.4$–$109.3$, while the energy rises by about 2.3 MeV above the minimum.
- The constrained β_{40} scan shows that **fluctuations beyond the two-dimensional shape space can provide additional mass broadening**.

Appendix: experimental studies of ^{180}Hg

Low-energy β-delayed fission

The decay of ^{180}Tl populates ^{180}Hg*, with accessible energies limited by $Q_{\mathrm{EC}} \approx 10.44$ MeV; the mass split is near $80/100$.

A. N. Andreyev et al., Phys. Rev. Lett. **105**, 252502 (2010).

J. Elseviers et al., Phys. Rev. C **88**, 044321 (2013).

Fusion-fission

$^{36}\mathrm{Ar} + {}^{144}\mathrm{Sm} \longrightarrow {}^{180}\mathrm{Hg}^*$: at moderate excitation energies, the asymmetric component still peaks near $79/101$.

K. Nishio et al., Phys. Lett. B **748**, 89 (2015).

E. M. Kozulin et al., Phys. Rev. C **105**, 014607 (2022).

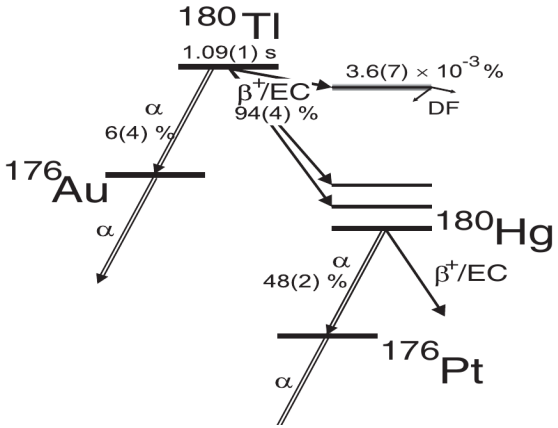
Entrance-channel effects

$^{68}\mathrm{Zn} + {}^{112}\mathrm{Sn}$ forms the same composite system, but the component near $68/112$ is strongly affected by quasifission.

E. M. Kozulin et al., Phys. Lett. B **819**, 136442 (2021).

E. Vardaci et al., EPJ Web Conf. **304**, 01003 (2024).

Appendix: ^{180}Tl decay and the low-energy fission channel



A. N. Andreyev et al., Phys. Rev. Lett. **105**, 252502 (2010).

Appendix: internal energy, entropy, and level density in finite-temperature BCS

Occupation numbers and pairing tensor

$$n_k^\tau = 1 - \frac{\varepsilon_k^\tau - \lambda_\tau}{E_k^\tau} \tanh\left(\frac{E_k^\tau}{2T}\right)$$

$$\kappa_k^\tau = \frac{\Delta_\tau}{2E_k^\tau} \tanh\left(\frac{E_k^\tau}{2T}\right)$$

Internal and intrinsic excitation energies

$$\mathcal{E}_\tau(T,q) = \sum_{k>0} \varepsilon_k^\tau n_k^\tau - \frac{\Delta_\tau^2}{G_\tau}$$

$$U_\tau = \mathcal{E}_\tau(T,q) - \mathcal{E}_\tau(0,q)$$

$$U = U_\nu + U_\pi = E^* - V(q)$$

Entropy and saddle-point approximation

$$S_\tau = -2\sum_{k>0} \left[f_k^\tau \ln f_k^\tau + (1-f_k^\tau)\ln(1-f_k^\tau)\right]$$

$$S = S_\nu + S_\pi, \qquad \rho_{\rm int} = \frac{e^S}{(2\pi)^{3/2}\mathcal{D}}$$

$\mathcal{D}$ is the square root of the thermodynamic-curvature determinant at the inverse-Laplace saddle point; neutrons and protons share one local temperature.

The zero-temperature shape landscape is fixed; finite-temperature intrinsic degrees of freedom set the statistical weights.

A. Rahmatinejad et al., Phys. Rev. C **103**, 034309 (2021); **105**, 044328 (2022).

A. Rahmatinejad et al., Eur. Phys. J. A **60**, 214 (2024).

Appendix: master equation, detailed balance, and scission probability flux

Fermi-golden-rule form

$$\Lambda_{ij} = \frac{2\pi}{\hbar}|\langle i|\hat{V}|j\rangle|^2 \rho_i \equiv \lambda_{ij}\rho_i$$

$$\lambda_{ij} = \lambda_{ji} = \frac{\lambda}{\sqrt{\rho_i \rho_j}}$$

Detailed balance

$$\Lambda_{ij}\rho_j = \Lambda_{ji}\rho_i, \qquad P_i^{\mathrm{eq}} \propto \rho_i$$

Here Λ_{ij} is the transition rate from j to i; the level density of the final state i enters Fermi's golden rule.

Cumulative probability at the absorbing boundary

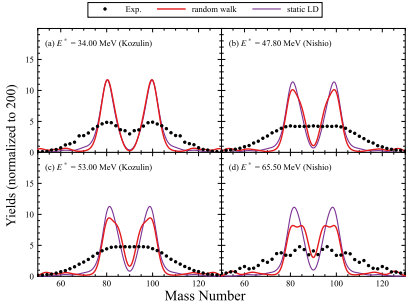
$$\mathcal{P}(i_s) = \int_0^\infty dt \sum_{j \notin \mathcal{S}} \Lambda_{i_s j} P_j(t)$$

- Random walk: records where each trajectory first reaches the scission line.
- Equilibrium reference: $P^{\mathrm{eq}}(i_s) = \rho_{i_s} / \sum_{i'_s} \rho_{i'_s}$.
- The original report used distinct rate scales for nucleon transfer and shape transitions; the present two-dimensional calculation uses a common scale λ.

L. G. Moretto and J. S. Sventek, Phys. Lett. B **58**, 26 (1975).

G. G. Adamian et al., Fiz. Elem. Chastits At. Yadra **25**, 1379 (1994).

Appendix: mass-distribution results presented in Dubna



Red: random walk Purple: static level-density weights Black symbols: experiment

This slide retains the earlier results for comparison; the main text shows the current results with $\sigma_A = 4.0\,\mathrm{u}$ broadening.

K. Nishio et al., Phys. Lett. B **748**, 89 (2015).

E. M. Kozulin et al., Phys. Rev. C **105**, 014607 (2022).

Appendix: meson-exchange RMF model

Relativistic mean-field Lagrangian

$$\mathcal{L} = \bar{\psi}(i\gamma_\mu\partial^\mu - M)\psi + \mathcal{L}_\sigma + \mathcal{L}_\omega + \mathcal{L}_\rho + \mathcal{L}_{\text{em}}.$$

$$\mathcal{L}_\sigma = \frac{1}{2}\partial_\mu\sigma\partial^\mu\sigma - \frac{1}{2}m_\sigma^2\sigma^2 - g_\sigma\sigma\bar{\psi}\psi - \frac{1}{3}g_2\sigma^3 - \frac{1}{4}g_3\sigma^4,$$

$$\mathcal{L}_\omega = -\frac{1}{4}\Omega_{\mu\nu}\Omega^{\mu\nu} + \frac{1}{2}m_\omega^2\omega_\mu\omega^\mu - g_\omega\omega_\mu\bar{\psi}\gamma^\mu\psi - \frac{1}{4}c_3(\omega_\mu\omega^\mu)^2,$$

$$\mathcal{L}_\rho = -\frac{1}{4}\boldsymbol{R}_{\mu\nu}\cdot\boldsymbol{R}^{\mu\nu} + \frac{1}{2}m_\rho^2\boldsymbol{\rho}_\mu\cdot\boldsymbol{\rho}^\mu - g_\rho\boldsymbol{\rho}_\mu\cdot\bar{\psi}\gamma^\mu\boldsymbol{\tau}\psi.$$

Physical roles of the fields

σ	Isoscalar–scalar attraction; reduces the Dirac effective mass.
ω	Isoscalar–vector repulsion; balances attraction and generates saturation.
ρ	Isovector–vector channel; affects neutron–proton asymmetry.
π	Contributes in relativistic Hartree–Fock; vanishes by parity in pure Hartree calculations.
δ	Isovector–scalar channel; relevant to exotic nuclei and dense matter.
γ	Electromagnetic Coulomb repulsion between protons.

A. Bouyssy et al., Phys. Rev. C **36**, 380 (1987).
P. Ring, Prog. Part. Nucl. Phys. **37**, 193 (1996).
B. N. Lu, Ph.D. thesis, ITP-CAS (2012).

Appendix: point-coupling formulation and self-consistent single-particle fields

From finite-range interactions to local densities

$$\sigma, \omega, \rho \quad \Longrightarrow \quad \rho_{\mathrm{S}},\ j^{\mu}_{\mathrm{V}},\ \boldsymbol{j}^{\mu}_{\mathrm{TV}},$$

Derivative terms simulate the finite-range effects of the interaction.

$$\mathcal{L}_{\mathrm{PC}} = \mathcal{L}_0 + \mathcal{L}_{4\mathrm{f}} + \mathcal{L}_{\mathrm{nl}} + \mathcal{L}_{\mathrm{der}} + \mathcal{L}_{\mathrm{em}}.$$

$$\mathcal{L}_{4\mathrm{f}} = -\frac{1}{2}\alpha_{\mathrm{S}}\rho_{\mathrm{S}}^2 - \frac{1}{2}\alpha_{\mathrm{V}} j_{\mathrm{V}\mu} j^{\mu}_{\mathrm{V}} - \frac{1}{2}\alpha_{\mathrm{TV}} \boldsymbol{j}_{\mathrm{TV}\mu} \cdot \boldsymbol{j}^{\mu}_{\mathrm{TV}},$$

$$\mathcal{L}_{\mathrm{nl}} = -\frac{1}{3}\beta_{\mathrm{S}}\rho_{\mathrm{S}}^3 - \frac{1}{4}\gamma_{\mathrm{S}}\rho_{\mathrm{S}}^4 - \frac{1}{4}\gamma_{\mathrm{V}}(j_{\mathrm{V}\mu} j^{\mu}_{\mathrm{V}})^2,$$

$$\mathcal{L}_{\mathrm{der}} = -\frac{1}{2}\delta_{\mathrm{S}}(\partial_\nu \rho_{\mathrm{S}})^2 - \frac{1}{2}\delta_{\mathrm{V}}(\partial_\nu j_{\mathrm{V}\mu})^2 - \frac{1}{2}\delta_{\mathrm{TV}}(\partial_\nu \boldsymbol{j}_{\mathrm{TV}\mu})^2.$$

Self-consistent Dirac Hamiltonian

$$h_{\mathrm{D}} = \boldsymbol{\alpha}\cdot\boldsymbol{p} + \beta[M + S(\boldsymbol{r})] + V(\boldsymbol{r}).$$

$$S(\boldsymbol{r}) = \alpha_{\mathrm{S}}\rho_{\mathrm{S}} + \beta_{\mathrm{S}}\rho_{\mathrm{S}}^2 + \gamma_{\mathrm{S}}\rho_{\mathrm{S}}^3 + \delta_{\mathrm{S}}\Delta\rho_{\mathrm{S}},$$

$$V(\boldsymbol{r}) = \alpha_{\mathrm{V}}\rho_{\mathrm{V}} + \gamma_{\mathrm{V}}\rho_{\mathrm{V}}^3 + \delta_{\mathrm{V}}\Delta\rho_{\mathrm{V}} + \alpha_{\mathrm{TV}}\rho_{\mathrm{TV}}\tau_3 + \delta_{\mathrm{TV}}\Delta\rho_{\mathrm{TV}}\tau_3 + e\frac{1-\tau_3}{2}A^0.$$

Application in this work

- No explicit solution of Klein–Gordon equations for meson fields is required.
- Fitted coupling constants absorb short-range correlations that are not treated explicitly.
- The potential energy, single-particle spectrum, and nucleon densities are obtained self-consistently on the same grid.

Appendix: main approximations in RMF/RHB

Mean-field and Hartree approximations

Meson-field operators are replaced by their expectation values:

$$\langle \partial_\mu \hat{\sigma}\, \partial^\mu \hat{\sigma} \rangle \to \partial_\mu \sigma\, \partial^\mu \sigma, \qquad \langle \hat{\sigma}\, \bar{\hat{\psi}} \hat{\psi} \rangle \to \sigma \langle \bar{\hat{\psi}} \hat{\psi} \rangle.$$

Direct Hartree terms are retained explicitly; exchange effects are treated phenomenologically through the parameters.

$$D_\phi(\boldsymbol{r}, \boldsymbol{r}') = \frac{e^{-m_\phi |\boldsymbol{r} - \boldsymbol{r}'|}}{4\pi |\boldsymbol{r} - \boldsymbol{r}'|}.$$

No-sea approximation

$$\hat{\psi}(x) = \sum_i \psi_i(x) c_i$$

Source densities explicitly include occupied positive-energy nucleon states; vacuum contributions from the Dirac sea are not summed explicitly.

Static even–even nucleus

For static, time-reversal-invariant $^{180}\mathrm{Hg}$:

- time derivatives vanish;
- spatial currents cancel pairwise;
- only the time components of vector fields remain.

$$\rho_{\mathrm{V}}(\boldsymbol{r}) = j^0_{\mathrm{V}}(\boldsymbol{r}), \qquad \rho_{\mathrm{TV}}(\boldsymbol{r}) = j^{0,3}_{\mathrm{TV}}(\boldsymbol{r}).$$

Pairing correlations: RHB equation

$$\begin{pmatrix} h_{\mathrm{D}} - \lambda & \Delta \\ -\Delta^* & -h^*_{\mathrm{D}} + \lambda \end{pmatrix} \begin{pmatrix} U_k \\ V_k \end{pmatrix} = E_k \begin{pmatrix} U_k \\ V_k \end{pmatrix}.$$

Pairing correlations are described by a Hartree–Bogoliubov quasiparticle vacuum.

Appendix: pairing structure of RHB

Bogoliubov transformation

Quasiparticle operators are defined as linear combinations of single-particle creation and annihilation operators:

$$\hat{\beta}_k^\dagger = \sum_l \left(U_{lk} \hat{c}_l^\dagger + V_{lk} \hat{c}_l \right), \qquad \hat{\beta}_k = \sum_l \left(U_{lk}^* \hat{c}_l + V_{lk}^* \hat{c}_l^\dagger \right).$$

The quasiparticle vacuum satisfies

$$\hat{\beta}_k |\Omega\rangle = 0, \qquad k = 1, 2, \cdots.$$

In a BCS-like canonical basis,

$$|\Omega\rangle \propto \prod_{k>0} \left(u_k + v_k \hat{c}_k^\dagger \hat{c}_{\bar{k}}^\dagger \right) |0\rangle, \qquad u_k^2 + v_k^2 = 1.$$

Density and pairing tensor in the energy functional

$$\rho_{ij} = \sum_k V_{ik}^* V_{jk}, \qquad \kappa_{ij} = \sum_k V_{ik}^* U_{jk}.$$

HB equation and its relativistic form

Variation of the energy under the particle-number constraint gives

$$\begin{pmatrix} h - \lambda & \Delta \\ -\Delta^* & -h^* + \lambda \end{pmatrix} \begin{pmatrix} U_k \\ V_k \end{pmatrix} = E_k \begin{pmatrix} U_k \\ V_k \end{pmatrix}.$$

The matrix elements are

$$h_{ij} = t_{ij} + \sum_{kl} V_{ikjl} \rho_{lk}, \qquad \Delta_{ij} = \frac{1}{2} \sum_{kl} V_{ijkl} \kappa_{kl}.$$

In the relativistic formulation, the Dirac single-particle Hamiltonian h_D replaces h.

H. Kucharek and P. Ring, Z. Phys. A **339**, 23 (1991).
B. N. Lu, Ph.D. thesis, ITP-CAS, Sec. 2.3.1 (2012).

Appendix: zero-temperature BCS limit and pairing force

BCS approximation in the canonical basis

When eigenstates of the single-particle Hamiltonian approximate the canonical basis, the occupation probability is

$$v_k^2 = \frac{1}{2}\left[1 - \frac{\epsilon_k - \lambda}{\sqrt{(\epsilon_k - \lambda)^2 + \Delta_k^2}}\right].$$

The gap and particle-number equations are

$$\Delta_k = \sum_{k'>0} G_{kk'} \frac{\Delta_{k'}}{2\sqrt{(\epsilon_{k'} - \lambda)^2 + \Delta_{k'}^2}},$$

$$\sum_{k>0} 2v_k^2 = N.$$

$G_{kk'}$ denotes the effective pairing matrix element in the convention of positive attractive strength. Zero-temperature BCS provides the reference for the finite-temperature level-density calculation.

Pairing field

The pairing tensor generates the pairing field in coordinate space:

$$\Delta_{p_1 p_2}(\boldsymbol{r}_1\sigma_1, \boldsymbol{r}_2\sigma_2) = \int d^3\boldsymbol{r}_1' d^3\boldsymbol{r}_2' \sum_{\sigma_1'\sigma_2'} V^{pp}_{p_1 p_2, p_1' p_2'} \kappa_{p_1' p_2'}.$$

We use the finite-range separable pairing force proposed by Tian, Ma, and Ring:

$$V^{pp}(\boldsymbol{r}_1, \boldsymbol{r}_2, \boldsymbol{r}_1', \boldsymbol{r}_2') = -G\,\delta(\boldsymbol{R} - \boldsymbol{R}')P(\boldsymbol{r})P(\boldsymbol{r}')\frac{1 - \hat{P}_\sigma}{2},$$

$$\boldsymbol{R} = \frac{\boldsymbol{r}_1 + \boldsymbol{r}_2}{2}, \quad \boldsymbol{r} = \boldsymbol{r}_1 - \boldsymbol{r}_2.$$

$$P(\boldsymbol{r}) = \frac{1}{(4\pi a^2)^{3/2}} \exp\left(-\frac{\boldsymbol{r}^2}{4a^2}\right).$$

This work: RHB treats the mean field and pairing correlations self-consistently. The MDC-RHB single-particle spectrum feeds the FT-BCS level-density calculation.

Y. Tian et al., Phys. Lett. B **676**, 44 (2009).
Y. Tian et al., Phys. Rev. C **80**, 024313 (2009).
B. N. Lu, Ph.D. thesis, ITP-CAS, Sec. 2.3.1 (2012).

Appendix: V_4 symmetry and deformation degrees of freedom

Symmetry allowing reflection-asymmetric shapes

$$V_4 = \{1, \hat{P}_x, \hat{P}_y, \hat{R}_z(\pi)\}$$

$$\rho(x, y, z) = \rho(-x, y, z) = \rho(x, -y, z) = \rho(-x, -y, z)$$

$\hat{P}_x$ and $\hat{P}_y$ denote reflections of the x and y coordinates. Invariance under $z \to -z$ is not required, so $\beta_{30} \neq 0$ is allowed.

Multipole moments and deformation parameters

$$\langle \hat{Q}_{\lambda\mu} \rangle = \int d^3 r \, \rho_V(\boldsymbol{r}) r^\lambda Y_{\lambda\mu}(\Omega)$$

$$\beta_{\lambda\mu} = \frac{4\pi}{3AR^\lambda} \langle \hat{Q}_{\lambda\mu} \rangle$$

Allowed multipole components

$$\mu = 0, 2, 4, \ldots \leq \lambda$$

Type	Examples	Physical role
Quadrupole	β_{20}, β_{22}	Axial/triaxial
Octupole	β_{30}, β_{32}	Reflection asymmetry
Hexadecapole	$\beta_{40}, \beta_{42}, \beta_{44}$	Higher-order shape

This work explicitly constrains $q = (\beta_{20}, \beta_{30})$; all other allowed, unconstrained deformations are determined variationally.

B.-N. Lu et al., Phys. Rev. C **89**, 014323 (2014).
S.-G. Zhou, Phys. Scr. **91**, 063008 (2016).
J. Zhao et al., Phys. Rev. C **95**, 014320 (2017).